Lawrence Berkeley National Laboratory

Title

Enhanced orbital anisotropy through the proximity to a SrTiO3 layer in the perovskite iridate superlattices

Permalink

https://escholarship.org/uc/item/21v0378f

Journal

Physical Review B, 104(7)

ISSN

2469-9950

Authors

Huang, Wencheng
Liu, Wanling
Shao, Yu-Cheng
et al.

Publication Date

2021-08-01

DOI

10.1103/physrevb.104.075156

Peer reviewed

Enhanced orbital anisotropy through the proximity to a SrTiO₃ layer in the perovskite iridate superlattices

Wencheng Huang [1,2,7,*], Wanling Liu [1,3], Yu-Cheng Shao,[2,4] Xuefei Feng,[2] Nian Zhang,[1] Jiamin Fu,[5]
Jenn-Min Lee [6], Dawei Shen,[1] Yi-De Chuang,[2,†] and Xiaosong Liu [1,3,‡,§]

[1]*State Key Laboratory of Functional Materials for Informatics, Shanghai Institute of Microsystem and Information Technology,
Chinese Academy of Sciences, Shanghai 200050, China*
[2]*Advanced Light Source, Lawrence Berkeley National Laboratory, Berkeley, California 94720, USA*
[3]*School of Physical Science and Technology, ShanghaiTech University, Shanghai 200031, China*
[4]*National Synchrotron Radiation Research Center, Hsinchu 300, Taiwan*
[5]*Department of Chemistry, University of Western Ontario, 1151 Richmond Street, London, Ontario N6A 5B7, Canada*
[6]*MAX IV Laboratory, Lund University, Lund 224 84, Sweden*
[7]*University of Chinese Academy of Sciences, Beijing 100049, China*

We have used angle-dependent soft x-ray absorption spectroscopy (XAS) at the O K edge and first-principles calculations to investigate the electronic structures of iridate-based superlattices $(SrIrO_3)_m/(SrTiO_3)$ ($m = 1, 2,$ 3, and ∞). We focus on the pre-edge Ir $5d$ t_{2g}–O $2p$ orbital hybridization feature in the XAS spectra. By varying the measurement geometry relative to the incident photon polarization, we are able to extract the dichroic contrast and observe the systematic increase in the anisotropy of Ir $5d$ orbitals as m decreases. First-principles calculations elucidate the orbital anisotropy coming mainly from the enhanced out-of-plane compression of IrO_6 octahedra in the $SrIrO_3$ layers that are adjacent to the inserted $SrTiO_3$ layers. As m decreases, the increased volume fraction of these interfacial $SrIrO_3$ layers and their contact with the $SrTiO_3$ layers within the $(SrIrO_3)_m/(SrTiO_3)$ supercell lead to enhanced orbital anisotropy. Furthermore, the tilt and rotation of IrO_6 octahedra are shown to be essential to understand the subtle orbital anisotropy in these superlattices, and constraining these degrees of freedom will give an incorrect trend. Our results demonstrate that the structural constraint from the inserted $SrTiO_3$ layers, in addition to other electronic means such as polar interface and charge transfer, can serve as a knob to control the orbital degree of freedom in these iridate-based superlattices.

I. INTRODUCTION

The strong spin-orbit coupling (SOC) in iridates with a nominal Ir 4+ valency ($5d^5$) can induce a Mott state with an effective total angular momentum $J_{\text{eff}} = 1/2$ [1,2]. This Mott state is proposed to be the origin of various interesting phenomena such as the topological insulator, axion insulator, Weyl semimetal, quantum spin liquid, etc. [3–8]. It may contrast with the spin $S = 1/2$ state in the strong U (Coulomb) $3d$ Mott insulators (e.g., cuprates) where the emergent properties such as high-temperature superconductivity, density waves, non-Fermi liquid behavior, quantum criticality, etc., are observed after the carrier doping [9–11]. This $J_{\text{eff}} = 1/2$ Mott state provides a new playground for exploring the response of correlated electronic structures to the varying degrees of fundamental interactions that might be similar to or distinct

from their $3d$ counterparts [12,13]. Besides using the carrier doping, heterostructure stacking has also been demonstrated as a powerful and versatile way to alter the relevant energy scales such as the electron itinerancy, exchange interaction, SOC, etc., in the system. Through this route, phenomena such as two-dimensional electron gases [14,15], ferromagnetism-superconductivity proximity [16], orbital polarization, and charge transfer [17–20], to name a few, can be manifested at the interfaces of heterostructures.

Iridate-based heterostructures formed with various $3d$ transition metal oxides have been widely studied and there are reports of electronic and magnetic reconstructions at the interfaces. These heterostructures often have factors such as strain, polar interfaces, strong Hund's rule coupling, oxygen vacancies, etc., to trigger and/or facilitate the reconstructions [21–27]. For the prototypical $(SrIrO_3)_m/(SrTiO_3)$ superlattices (SLs) comprised of m layers of SrIrO₃ (SIO) and one layer of SrTiO₃ (STO) in the supercell [see the schematic illustration in Fig. 1(a)], their constituents are nonpolar and the interfacial charge transfer is not expected [20,28,29]. The strain from the lattice mismatch between SIO and STO is expected to be the main factor for causing the electronic reconstruction in these SLs. However, the resulting Ir $5d$ orbital anisotropy seen in our O K-edge soft x-ray absorption

---
[*]wenchenghuang@lbl.gov
[†]ychuang@lbl.gov
[‡]xsliu19@ustc.edu.cn
[§]Present address: National Synchrotron Radiation Laboratory, University of Science of Technology of China, Hefei, Anhui 230029, China.
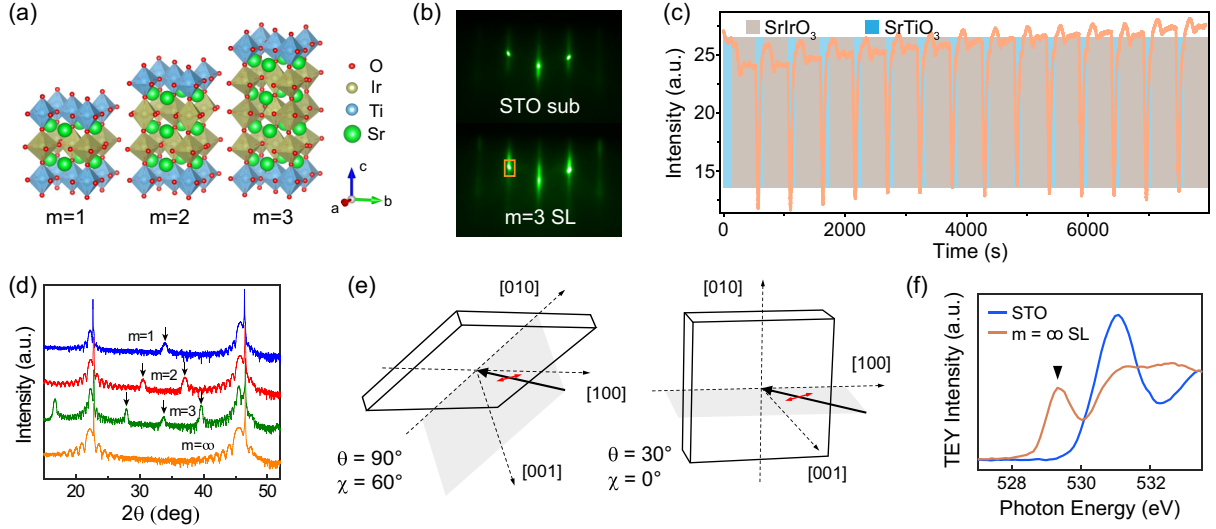
FIG. 1. (a) Schematic plot showing the stacking of SrIrO$_3$ (yellow) and SrTiO$_3$ (blue) layers to form the (SrIrO$_3$)$_m$/(SrTiO$_3$) superlattice. (b) The RHEED patterns of (001)-oriented STO substrate (top) and the $m = 3$ SL (bottom). (c) Time dependence of the RHEED intensity curve of [01] diffraction spots [orange box in panel (b)] of the $m = 3$ SL. (d) The XRD θ-2θ scans of SLs with $m = 1, 2, 3$, and ∞. Arrows indicate the superlattice peaks. (e) Schematic plot showing the experimental geometry and sample angles (θ and χ) relative to the incident x-ray beam. The red arrow denotes the linear photon polarization. (f) TEY mode of O K-edge XAS spectra from the $m = \infty$ SL (yellow curve) and SrTiO$_3$ (blue curve) substrate. The inverted triangle denotes the Ir t_{2g}-O p hybridization feature.

spectra (XAS) is rather subtle and exhibits different behaviors between the near-surface and the near-substrate regions.

Near the surface region, there is more spectral weight in the unoccupied density of states (DOS) for the out-of-plane Ir $5d$ orbital components (yz and xz) than the in-plane component (xy). This anisotropy displays a systematic increase with decreasing m. Beyond the surface region, the magnitude of orbital anisotropy is reduced. For the $m = \infty$ SL, the sign of orbital anisotropy is even reversed. First-principles calculations suggest that the orbital anisotropy mainly comes from the interfacial SIO layers adjacent to the inserted STO layers, which experience an enhanced compression along the z axis. As their coordination to the STO layers and the volume fraction in the supercell increase with decreasing m, so does the overall orbital anisotropy.

II. EXPERIMENTS

The orthorhombic perovskite SIO/STO SL films with $m = 1, 2, 3$, and ∞ were grown on SrTiO$_3$(001) substrate using a molecular beam epitaxy (MBE) system (DCA R450). In the epitaxial growth process, the substrate temperature was set to 620 °C, and the growth was performed in a distilled ozone atmosphere with 2.5×10^{-6} Torr pressure. Strontium and titanium were evaporated from the thermal Knudsen cells, and iridium was evaporated from an electron beam evaporator. Their fluxes were checked by a quartz crystal microbalance before and after the deposition to ensure a constant deposition rate. Figure 1(b) shows the typical reflection high-energy electron diffraction (RHEED) patterns for (001)-oriented SrTiO$_3$ substrate (top panel) and $m = 3$ SL (bottom panel). The RHEED images exhibit sharp streaks without extra diffraction spots, indicating the perfect surface for $m = 3$ SL. A typical RHEED intensity curve for the [01] diffraction rod [the orange square in Fig. 1(b)] is shown in Fig. 1(c).

Oscillations highlighted by light blue and light gray represent the growth periods of STO and SIO layers, respectively. The uniform periodicity and the relatively stable amplitude in the RHEED oscillation curve throughout the deposition demonstrate the persistent layer by layer growth of SLs. From the RHEED oscillations, the thickness of $m = 1, 2, 3$, and ∞ SLs is determined to be approximately 14.4, 13.2, 24, and 16 nm, respectively. Note that the $m = \infty$ SL is actually a bilayer [there is no STO in the supercell, so the conventional notation is ∞]. Figure 1(d) shows the x-ray diffraction (XRD) $\theta - 2\theta$ scans of all samples. In this figure, the arrows mark the superlattice peaks. These characterizations affirm the high quality of SLs used in the current study.

O K-edge XAS measurements were performed at Beamline 8.0.1 at the Advanced Light Source (ALS), Lawrence Berkeley National Laboratory; Beamline 20A at the Taiwan Light Source, National Synchrotron Radiational Research Center (NSRRC); and Beamline 02B at the Shanghai Synchrotron Radiation Facility (SSRF) [30]. The results from these facilities are consistent with each other and in this paper, we only show the data from the ALS. The XAS spectra were recorded in both total electron yield mode (TEY XAS, with probe depth around 5 nm, sample to ground drain current) and total fluorescence yield mode (TFY XAS, with probe depth around 100 nm; the signal from an Al-coated GaAsP photodiode was placed at 30° backscattering angle relative to the incident x-ray beam). The recorded spectra normalized to the incident photon flux were first subtracted by the background in the [520, 526 eV] energy window (pre-edge) followed by scaling the spectral weight at 564 eV (postedge) to 1. During the measurements, the samples were kept at 300 K and the beamline energy resolution was set to 0.3 eV. The samples were azimuthally aligned such that the Ir-O bond direction was in the horizontal scattering plane, the same as the linear photon polarization (π polarization). To vary the

photon polarization projection on the sample surface without changing the probed SIO/STO SL volume, hence mitigating the angle-dependent self-absorption effect that could arise in the TFY XAS spectra, the sample polar (θ) and flip (χ) angles were set to (90°, 60°) and (30°, 0°), respectively [see Fig. 1(e) for the experimental geometry].

For first-principles calculations, we used the projector-augmented wave (PAW) method [31] and the Perdew-Burke-Ernzerhof (PBE) exchange-correlation potential within the general gradient approximation (GGA) [32], as implemented in the Vienna *ab initio* simulation package (VASP) [33]. To take into account the correlation effect and the strong SOC in Ir $5d$ orbitals, we used the GGA+U+SOC method with an effective U value of 2 eV ($U_{\mathrm{eff}} = U - J$) [34,35]. The valence electrons were described by a plane-wave basis set with an energy cutoff of 600 eV. The convergence criterion on the total energy was 1×10^{-5} eV. Monkhorst-Pack k meshes for $m = 1, 2, 3$, and ∞ SLs were $7 \times 7 \times 5$, $7 \times 7 \times 2$, $7 \times 7 \times 3$, and $7 \times 7 \times 5$, respectively. For structural relaxations, 0.01 eV/Å was used for the force convergence tolerance. Canted ab-AF ordering was imposed for all SLs to represent the ground state magnetic structure [25,36]. Since the tilt and rotation angles of IrO$_6$ octahedra are sizable from the calculations, the projection of DOS onto Ir $5d$ orbitals is performed on the local coordinate system of the corresponding IrO$_6$ octahedron.

III. RESULTS AND DISCUSSIONS

A. XAS measurements

The O K-edge TEY XAS spectra from the STO substrate (blue line) and the $m = \infty$ SL (yellow line) taken at (θ, χ) = (90°, 0°) are shown in Fig. 1(f). Comparing these two spectra, we see that the $m = \infty$ SL has a pronounced pre-edge feature at 529.4 eV, which comes from the hybridization between Ir $5d$ t_{2g} and O $2p$ orbitals (referred to as Ir t_{2g} in this paper) [37–39]. With low spin configuration, the Ir e_g–O $2p$ hybridization feature (referred to as Ir e_g) will situate at higher energy around 531–532 eV and overlap with the strong Ti $3d$ t_{2g}–O $2p$ hybridization peak (referred to as Ti t_{2g}) at 531 eV. To facilitate the identification of orbital anisotropy, we only focus on this Ir t_{2g} feature to examine the response of Ir orbitals to the superlattice stacking.

Figure 2(a) shows the angle-dependent O K-edge TEY XAS spectra of SIO/STO SLs recorded at two different geometries: $\theta = 90°$ (black line, completely in-plane photon polarization) and 30° (red line; photon polarization has a large out-of-plane projection). For the $m = \infty$ SL, we see little difference in the Ir t_{2g} feature between these two spectra, suggesting the nearly isotropic Ir $5d$ t_{2g} orbitals. However, as m decreases, the difference increases and the Ir t_{2g} feature exhibits more spectral weight at a smaller polar angle θ. Since the photon polarization will enhance the out-of-plane orbital component (yz and xz) relative to the in-plane one (xy) when going from a larger to a smaller θ, the observed angle dependence in Fig. 2(a) suggests a noticeable Ir orbital anisotropy with more unoccupied DOS spectral weight in the yz/xz orbitals than the xy orbital for smaller m. Interestingly, the orbital anisotropy is much weaker in the TFY XAS spectra in Fig. 2(b) and for the $m = \infty$ SL, the sign is even reversed.
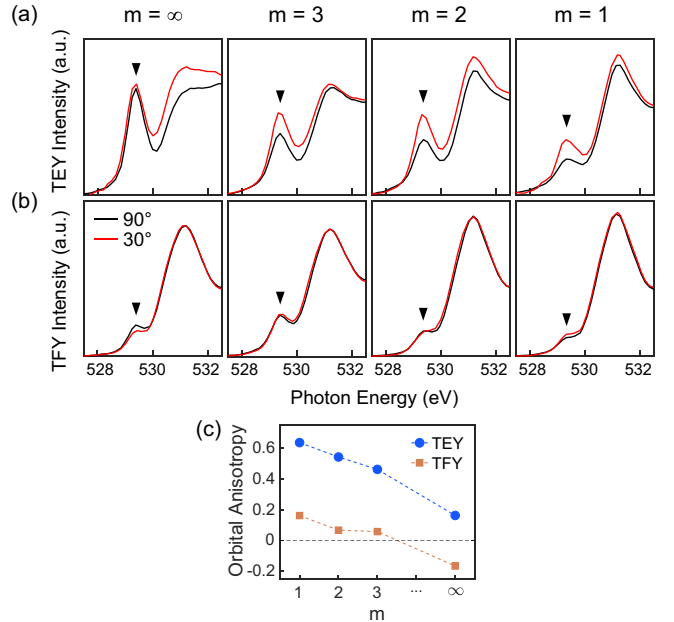

FIG. 2. O K-edge XAS spectra recorded in (a) TEY and (b) TFY modes. The inverted triangles mark the Ir-O hybridization feature. The red (30°) and black curves (90°) are from samples with photon polarizations projected largely out-of-plane and completely in-plane, respectively. (c) Orbital anisotropy calculated from the XAS recorded in the TEY (blue circles) and TFY (yellow squares) modes.

We notice that TEY and TFY modes of XAS have disparate probe depths with the former being far more surface sensitive than the latter. The different dichroic effects seen in Figs. 2(a) and 2(b) highlight the contrasting electronic structures around the surface and the heteroepitaxial interface regions of the SLs [40]. This probe depth difference is also reflected in the enhanced Ti t_{2g} feature in the TFY XAS spectra, which contains an additional contribution from the STO substrate. Figure 2(a) may suggest certain dichroic contrast for the Ir e_g orbitals around 531–532 eV, particularly for SLs with $m = 1$ and 2. However, such a phenomenon is absent in the bulk-sensitive TFY XAS spectra in Fig. 2(b). Furthermore, prior TEY XAS spectra from these SLs only showed the dichroic contrast in the Ir t_{2g} feature (data not shown), implying that the observed dichroic effect around 531 eV in Fig. 2(a) is extrinsic and likely caused by the surface absorbents when the samples were exposed to air between the experimental runs.

In the SLs, the Ir $5d$ t_{2g} orbitals can hybridize with different O $2p$ orbitals: the xy orbital hybridizes with four in-plane O $2p_x$ and $2p_y$ orbitals while the yz (xz) orbital hybridizes with two apical O $2p_y$ ($2p_x$) and two in-plane O $2p_z$ ($2p_z$) orbitals [39]. Different O $2p$ orbitals hybridized with Ir $5d$ orbitals (out-of-plane Ti-O-Ir and Ir-O-Ir, and in-plane Ir-O-Ir) can be excited by x rays and show up below the main O absorption peaks (530–532 eV). Although limited by the experimental energy resolution to differentiate the excitations into distinct O $2p$ orbitals in the pre-edge region, the linear dichroism seen in Fig. 2 can still give us the information of relative occupations between the Ir in-plane and out-of-plane orbitals

TABLE I. The Ir-O (Ti-O) bond lengths (in Å) of IrO_6 (TiO_6) octahedra in the SLs with $m = 1, 2, 3$, and ∞ for the region near the surface. The bonds are separated into three categories: STO layer, SIO layer adjacent to (interfacial), and away from (sandwiched) the STO layer. In each category, the first four numbers are the lengths of in-plane bonds and the last two numbers in bold are the out-of-plane bonds.

	SIO layer adjacent to the STO layer	SIO layer away from the STO layer
$m = 1$	2.036, 2.035, 2.036, 2.035, **2.023, 2.023**	
$m = 2$	2.034, 2.033, 2.040, 2.043, **2.042, 2.017**	
$m = 3$	2.043, 2.043, 2.042, 2.038, **2.049, 2.024**	2.042, 2.041, 2.042, 2.041, **2.042, 2.042**
$m = \infty$		2.053, 2.053, 2.053, 2.053, **2.040, 2.040**
	STO layer	
$m = 1$	1.976, 1.976, 1.976, 1.976, **1.962, 1.962**	
$m = 2$	1.955, 1.953, 2.011, 2.011, **1.964, 1.964**	
$m = 3$	1.992, 1.992, 1.994, 1.994, **1.965, 1.965**	
$m = \infty$		

concerning the stacking order m. Another aspect is that the fraction of Ti-O-Ir bonds in all Ir-O bonds decreases with increasing m, concurrently with the orbital anisotropy. This trend implies that the orbital anisotropy may be extremely localized at the SIO/STO interface.

B. Orbital anisotropy

To quantitively analyze the degree of orbital anisotropy, we follow the approach in Ref. [41]. We consider the dipole transition probability from O $1s$ to $2p$ orbitals, which is the same for transitions into p_x, p_y, and p_z orbitals [42]. The orientation factor is considered such that the measured spectral intensity I is a combination of spectra with photon polarization purely in-plane ($I_\parallel$) and out-of-plane ($I_\perp$): $I = I_\parallel \cos^2(\theta) + I_\perp \sin^2(\theta)$. Here, θ is the incidence angle of x rays relative to the sample surface. To avoid ambiguity and simplify the calculations amid the different Ir-O bonds for different O atoms in the supercell (see Table I), we do not consider the variations in the magnitude of pd orbital hybridization with m, which is assumed to be bond length dependent in the literature [40]. Under this assumption, the pd hybridization is set to be the same for π bonding between O p_x and Ir d_{xy} and d_{xz} (this notion holds for permuting the x, y, and z indices in the argument). Following this simplification, we only consider the D_{4h} symmetry and treat the xz and yz orbitals the same. This simplification is justified by the negligible difference between the DOS of xz and yz orbitals in Figs. 3(e)–3(p).

With these assumptions, the unoccupied DOS (neglecting the proportional factor here) will be proportional to the measured spectra:

$$h_z = \left(\frac{2}{3}\right)I_{30} - \left(\frac{1}{6}\right)I_{90},$$

$$h_{xy} = I_{90} - h_z.$$

Here, h_z (h_{xy}) is the hole occupation in the xz/yz (xy) orbitals. I_{30} and I_{90} are the spectra recorded at $\theta = 30°$ and $90°$, respectively. The orbital anisotropy P is defined as

$$P = \frac{h_z - h_{xy}}{h_z + h_{xy}}.$$

This orbital anisotropy, obtained from integrating the spectral weight in the [529, 530 eV] energy window in TEY XAS (blue circles) and TFY XAS (red squares) spectra, is plotted

in Fig. 2(c). The monotonic decreasing trend with increasing m is clearly seen in this figure.

C. DFT calculations for the near-surface region

To gain further insight into the origin of the orbital anisotropy and the difference between the results from TEY XAS and TFY XAS spectra, we resort to the first-principles calculations. In the calculations, we allowed the crystal structures to be fully relaxed to simulate the near-surface region. Since the pristine STO and SIO have the in-plane lattice constants of 3.905 and 3.94 Å, respectively, when forming the SLs, one would expect the compressive strain exerted by the STO layers onto the SIO layers. However, we found that the lengths of in-plane Ir-O bonds are still longer than those of the Ti-O bonds, similar to the single crystals. Achieving the longer Ir-O bonds in the SLs is accommodated by different degrees of IrO_6 octahedral tilt and in-plane rotation relative to the STO layers (see later discussion). The obtained total DOS and the projected DOS (PDOS) of Ir (blue line) and O (red line) atoms are shown in Figs. 3(a)–3(d), respectively. In these figures, the total Ir ($5d$) and O ($2p$) DOS in all SLs exhibit nearly identical profiles near the Fermi level, which is the outcome of the strong Ir-O orbital hybridization. As m increases, the bands near the Fermi level broaden and the band gap decreases monotonically, in agreement with the trend in the conductivity [25].

In Figs. 3(e)–3(h), we further project the total Ir DOS onto its five $5d$ orbitals. For each SL, within a 1 eV energy window centered at the Fermi energy, the PDOS of the out-of-plane yz and xz components are all larger than the in-plane xy component, consistent with the findings in Fig. 2(a). This anisotropy is due to the longer in-plane Ir-O bonds (2.033– 2.053 Å) than the out-of-plane bonds (2.017–2.049 Å) despite the compressive strain from the nearby STO layer with even shorter Ti-O bonds (see Table I). Moreover, the enhanced orbital anisotropy with respect to the decreased m can also be seen in the PDOS plots. To highlight this trend, the calculated orbital anisotropy using the aforementioned formula and the integrated PDOS spectral weight over the [0, 1 eV] energy window is summarized in Fig. 4(c) (red inverted triangles).

Unlike the consensus that the strain in heterostructures may decay over a characteristic length scale that depends on the degree of lattice mismatch between the constituents,
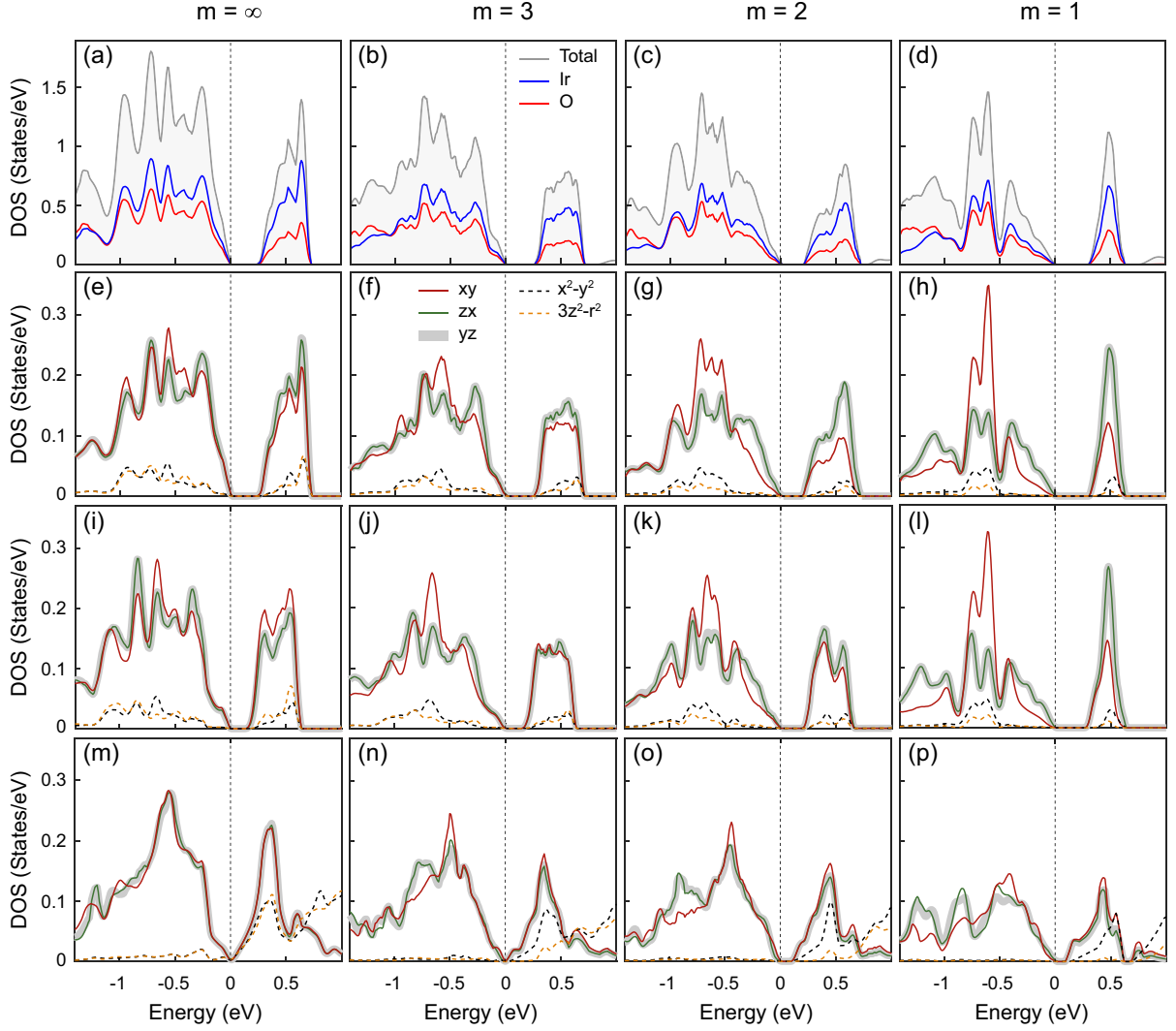
FIG. 3. Calculated density of states (DOS) for SLs with $m = \infty$ [(a), (e), (i), (m)], 3 [(b), (f), (j), (n)], 2 [(c), (g), (k), (o)], and 1 [(d), (h), (l), (p)]). (a)–(d) The total DOS (gray line) and PDOS on the Ir (blue line) and O (red line) elements. (e)–(p) Projected Ir DOS onto its five $5d$ orbitals [xy (red solid line), yz (gray solid line), xz (green solid line), $x^2 - y^2$ (black dashed line), and $3z^2 - r^2$ (orange dashed line)] for three cases: (e)–(h) for SLs close to the surface region where no constraint is applied to either the in-plane rotation/tilt degrees of freedom or lattice constants; (i)–(l) for SLs close to the STO substrate where the in-plane lattice constant of SLs is set to that of the pristine $SrTiO_3$, but the in-plane rotation/tilt degrees of freedom are permitted during the structural relaxation; (m)–(p) with constraint only on the in-plane rotation and tilt degrees of freedom of IrO_6 and TiO_6 octahedra. The Fermi energy is set to zero (black dashed line). The total DOS and PDOS are normalized by the number of oxygens in the supercell.

our calculations show that the response of IrO_6 octahedra to the inserted STO layers is highly layer dependent in these SLs. This, for example, can be clearly seen from the top and side views of the relaxed structures for $m = 1$ and 3 SLs in Fig. 4(a).

For $m = 1$ SL, the SIO layer sees STO layers above and below it, and this proximity limits the tilting of the IrO_6 octahedra such that the Ir-O-Ti bond angle is very close to $180°$. To sustain the longer in-plane Ir-O bonds, the in-plane rotation angle of IrO_6 octahedra increases to $14.1°$ [bottom panel, Fig. 4(a)]. The IrO_6 octahedra are compressed vertically, leading to two shorter out-of-plane bonds and four longer, nearly equal in-plane bonds. This distortion produces the largest orbital anisotropy among the SLs. For the $m = 2$ SL, we see that the IrO_6 octahedron is distorted asymmetri-

cally: the Ir-O bond towards the STO (SIO) layer becomes the shortest (longest).

Such complex structural distortion remains visible in the $m = 3$ SL, but only for the two SIO layers that are adjacent to the STO layers (interfacial layer, shaded yellow). The SIO layer sandwiched in between the interfacial SIO layers (sandwiched layer, shaded orange) behaves differently [right panel, Fig. 4(a)]. Similar to the $m = 1$ SL, the tilt angle of IrO_6 octahedra in the interfacial SIO layers is constrained by the contacting STO layers. As a result, the in-plane rotation angle is also very large [$11.4°$, right panel, Fig. 4(a)]. The distorted IrO_6 octahedra still produce discernible orbital anisotropy; see PDOS in the top panel of Fig. 4(d). However, for the sandwiched SIO layer, the in-plane rotation angle becomes smaller ($9.8°$) at the expense of a larger tilt angle. Interestingly, the
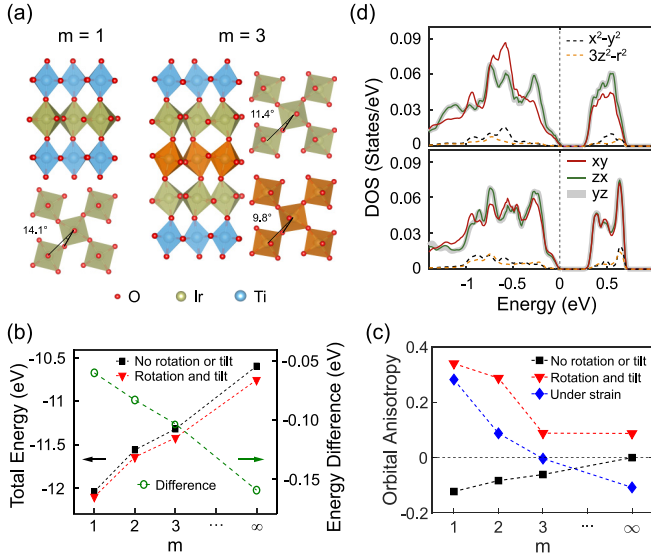
FIG. 4. (a) Side view and top view of $m = 1$ (left) and 3 (right) SLs with fully relaxed structure without strain. The shaded blue, orange, and yellow octahedra denote the TiO_6, IrO_6 (interfacial), and IrO_6 (sandwiched), respectively. The in-plane rotation angles are listed in the figure. (b) Calculated total energies (red triangles and black squares for results with and without IrO_6 octahedra tilt and in-plane rotation, respectively, left axis) and their difference (green open circles, right axis) as a function of m after the structural relaxation. The total energy is normalized by the number of oxygens in the supercell. (c) Calculated orbital anisotropy as a function of m for the following cases: with tilt and rotation, no strain (red triangles); without tilt and rotation, no strain (black squares); with tilt, rotation, and strain (blue diamonds). (d) Ir $5d$ PDOS for the interfacial (top) and sandwiched (bottom) SIO layer in $m = 3$ SL shown in panel (a). The Fermi energy is set to zero (black dashed line). The PDOS is averaged over all Ir sites lied in the same layer in the supercell.

IrO_6 volume expands and relaxes into a nearly perfect octahedron (see Table I) and this relaxation quenches the orbital anisotropy [bottom panel, Fig. 4(d)]. The contrasting behavior in the PDOS suggests that the tilt and rotation of the interfacial IrO_6 octahedra can effectively block the strain imposed by the STO layers and protect the sandwiched SIO layers, and the nearly absent orbital anisotropy in these sandwiched layers manifests a leveling of the decreasing trend around $m = 3$ in Fig. 4(c).

D. Constraining the in-plane lattice constants

Following the calculations for the near-surface region, we carried out another set of calculations to simulate the region close to the STO substrate. In this case, the in-plane lattice constants were fixed to that of the pristine STO while the out-of-plane lattice constant as well as the IrO_6 octahedral tilt and rotation degrees of freedom was allowed to change for the structural optimization. The obtained PDOS are shown in Figs. 3(i)–3(l). In the calculations, we found that the response of IrO_6 octahedra to the inserted STO layers is very similar to the previous case and the degree of orbital anisotropy also increases with decreasing m. This behavior is highlighted in the calculated orbital anisotropy in Fig. 4(c) (blue diamonds).

However, the magnitude of orbital anisotropy is reduced such that for $m = \infty$ SL, the sign is even reversed. This sign reversal is consistent with the results from TFY XAS that also probes the near-substrate region [Fig. 2(b)].

The reduced orbital anisotropy is the outcome of the competition from the valency difference between the in-plane and out-of-plane oxygens. The distinction between the two simulations indicates that the substrate strain imposed by mechanically clamping the SLs can be an important factor for understanding the complex behavior of the subtle orbital anisotropy and may shed light on the importance of carrying out similar studies on substrate-free SLs. One should also note that the broken translation symmetry at the surface of SLs can cause orbital reconstruction, which is not considered in the current study and may also contribute to the dichroic effect in TEY XAS [43].

E. Importance of IrO_6 octahedral tilt and rotation

In the previous calculations, we see that irrespective of constraining the in-plane lattice constants, the subtle orbital anisotropy still exhibits very similar m dependence except for the magnitude. The IrO_6 octahedra in the interfacial layers will respond to the compressive strain from the inserted STO layers by incurring different degrees of tilt and rotation to quickly screen the strain from propagating into the deeper SIO layers. Such octahedral tilt and rotation behaviors have been reported in other transition metal oxide heterostructures, and the associated concept of octahedral connectivity has been used to predict the materials' properties [44]. To show that these two degrees of freedom are indeed essential for understanding the observed orbital anisotropy, we repeat the simulations of the near-surface region except now these two degrees of freedom are set to 0.

In Fig. 4(b), we show the total energy of SLs without (black squares) and with (red triangles) the IrO_6 octahedral tilt/rotation. As expected, the relaxed structure will favor having these two degrees of freedom to accommodate the disparate Ir-O and Ti-O bond lengths to lower the total energy. The difference in total energy (green circles, right axis) increases monotonically with m, implying the importance of considering these two degrees of freedom as m increases. By eliminating them, the obtained PDOS in Figs. 3(m)–3(p) still show weak orbital anisotropy whose magnitude decreases as m increases. But unlike the results in Figs. 3(e)–3(h) (no substrate strain, with tilt/rotation, simulating the near-surface region) and Figs. 3(i)–3(l) (with substrate strain, with tilt/rotation, simulating the near-substrate region), the calculated orbital anisotropy from PDOS in Figs. 3(m)–3(p) has an opposite sign: The unoccupied states have a larger xy component than the yz/xz components [black squares, Fig. 4(c)]. This finding, contrary to the observed XAS spectra, is in fact expected from the crystal field picture as constraining these two degrees of freedom leads to the elongated out-of-plane (shortened in-plane) Ir-O bonds and lowers (raises) the energies of yz/xz (xy) orbitals. This shows that the crystal field picture, although simple and likely to be used as the first-order understanding, may miss important physics and yield incorrect predictions on materials' properties.

F. Summary

Our O K-edge XAS measurements and first-principles calculations reveal the evolution of local environments and electronic structures of SIO/STO SLs as the stacking sequence m is varied. We see that the suppressed tilting of IrO_6 octahedra in the interfacial SIO layers leads to the enhanced IrO_6 distortion, which is the main source of the subtle orbital anisotropy. As m decreases, the increased volume fraction of interfacial SIO layers in the supercell and their contact with STO layers lead to the monotonic increase of the orbital anisotropy. In that regard, one can envision manipulating the stacking of constituent layers in heterostructures to preferentially enhance or suppress the orbital response when other electronic means such as polar catastrophe, charge transfer, local magnetic moments, etc., are not available in the system [44,45]. Additionally, the difference in the overall orbital anisotropy between the near-surface and substrate regions of the SIO/STO SLs points to a nontrivial epitaxial strain effect. It has been shown that the interfacial electronic structures such as the spatial extension of charge transfer induced metallic layer can be controlled by the epitaxial strain [46], and undoubtedly, the substrate strain has been used as a powerful way to tune the overlayer properties. Our calculations that incorporate the tilt and in-plane rotation of IrO_6 octahedra under the strained condition go beyond the simple crystal field picture and correctly reproduce the TEY XAS and TFY XAS results. This effort emphasizes the need of addressing the substrate strain effect to properly apply the physics learned from the substrate-based thin-film/heterostructures to the free-standing or heteroepitaxy counterparts that are more applicable to the real device applications [47–50].

[1] B. J. Kim, H. Jin, S. J. Moon, J.-Y. Kim, B.-G. Park, C. S. Leem, J. Yu, T. W. Noh, C. Kim, S.-J. Oh, J.-H. Park, V. Durairaj, G. Cao, and E. Rotenberg, Phys. Rev. Lett. **101**, 076402 (2008).

[2] G. Jackeli and G. Khaliullin, Phys. Rev. Lett. **102**, 017205 (2009).

[3] W. Witczak-Krempa, G. Chen, Y. B. Kim, and L. Balents, Annu. Rev. Condens. Matter Phys. **5**, 57 (2014).

[4] J. G. Rau, E. K.-H. Lee, and H.-Y. Kee, Annu. Rev. Condens. Matter Phys. **7**, 195 (2016).

[5] L. Hao, D. Meyers, M. P. M. Dean, and J. Liu, J. Phys. Chem. Solids **128**, 39 (2019).

[6] Y. K. Kim, O. Krupin, J. D. Denlinger, A. Bostwick, E. Rotenberg, Q. Zhao, J. F. Mitchell, J. W. Allen, and B. J. Kim, Science **345**, 187 (2014).

[7] B. J. Kim, H. Ohsumi, T. Komesu, S. Sakai, T. Morita, H. Takagi, and T. Arima, Science **323**, 1329 (2009).

[8] S. Boseggia, R. Springell, H. C. Walker, H. M. Rønnow, Ch. Rüegg, H. Okabe, M. Isobe, R. S. Perry, S. P. Collins, and D. F. McMorrow, Phys. Rev. Lett. **110**, 117207 (2013).

[9] B. Keimer and J. E. Moore, Nat. Phys. **13**, 1045 (2017).

[10] B. Keimer, S. A. Kivelson, M. R. Norman, S. Uchida, and J. Zaanen, Nature (London) **518**, 179 (2015).

[11] C. Proust and L. Taillefer, Annu. Rev. Condens. Matter Phys. **10**, 409 (2019).

[12] J. Bertinshaw, Y. K. Kim, G. Khaliullin, and B. J. Kim, Annu. Rev. Condens. Matter Phys. **10**, 315 (2019).

[13] F. Wang and T. Senthil, Phys. Rev. Lett. **106**, 136402 (2011).

[14] S. Stemmer and S. J. Allen, Annu. Rev. Mater. Res. **44**, 151 (2014).

[15] M. Salluzzo, J. C. Cezar, N. B. Brookes, V. Bisogni, G. M. De Luca, C. Richter, S. Thiel, J. Mannhart, M. Huijben, A. Brinkman, G. Rijnders, and G. Ghiringhelli, Phys. Rev. Lett **102**, 166804 (2009).

[16] A. I. Buzdin, Rev. Mod. Phys. **77**, 935 (2005).

[17] Z. Liao, E. Skoropata, J. W. Freeland, E.-J. Guo, R. Desautels, X. Gao, C. Sohn, A. Rastogi, T. Z. Ward, T. Zou, T. Charlton, M. R. Fitzsimmons, and H. N. Lee, Nat. Commun. **10**, 589 (2019).

[18] S. Lee, A. T. Lee, A. B. Georgescu, G. Fabbris, M.-G. Han, Y. Zhu, J. W. Freeland, A. S. Disa, Y. Jia, M. P. M. Dean, F. J. Walker, S. Ismail-Beigi, and C. H. Ahn, Phys. Rev. Lett. **123**, 117201 (2019).

[19] J. Chakhalian, J. W. Freeland, H.-U. Habermeier, G. Cristiani, G. Khaliullin, M. van Veenendaal, and B. Keimer, Science **318**, 1114 (2007).

[20] H. Chen and A. Millis, J. Phys.: Condens. Matter **29**, 243001 (2017).

[21] D. Yi, C. L. Flint, P. P. Balakrishnan, K. Mahalingam, B. Urwin, A. Vailionis, A. T. N'Diaye, P. Shafer, E. Arenholz, Y. Choi, K. H. Stone, J.-H. Chu, B. M. Howe, J. Liu, I. R. Fisher, and Y. Suzuki, Phys. Rev. Lett. **119**, 077201 (2017).

[22] D. Yi, J. Liu, S.-L. Hsu, L. Zhang, Y. Choi, J.-W. Kim, Z. Chen, J. D. Clarkson, C. R. Serrao, E. Arenholz, P. J. Ryan, H. Xu, R. J. Birgeneau, and R. Ramesh, Proc. Natl. Acad. Sci. USA **113**, 6397 (2016).

[23] J. Nichols, X. Gao, S. Lee, T. L. Meyer, J. W. Freeland, V. Lauter, D. Yi, J. Liu, D. Haskel, J. R. Petrie, E.-J. Guo, A. Herklotz, D. Lee, T. Z. Ward, G. Eres, M. R. Fitzsimmons, and H. N. Lee, Nat. Commun. 7, 12721 (2016).

[24] X. Liu, M. Kotiuga, H.-S. Kim, A. T. N'Diaye, Y. Choi, Q. Zhang, Y. Cao, M. Kareev, F. Wen, B. Pal, J. W. Freeland, L. Gu, D. Haskel, P. Shafer, E. Arenholz, K. Haule, D. Vanderbilt, K. M. Rabe, and J. Chakhalian, Proc. Natl. Acad. Sci. USA 116, 19863 (2019).

[25] J. Matsuno, K. Ihara, S. Yamamura, H. Wadati, K. Ishii, V. V. Shankar, H.-Y. Kee, and H. Takagi, Phys. Rev. Lett. 114, 247209 (2015).

[26] L. Hao, D. Meyers, C. Frederick, G. Fabbris, J. Yang, N. Traynor, L. Horak, D. Kriegner, Y. Choi, J.-W. Kim, D. Haskel, P. J. Ryan, M. P. M. Dean, and J. Liu, Phys. Rev. Lett. 119, 027204 (2017).

[27] D. Meyers, Y. Cao, G. Fabbris, N. J. Robinson, L. Hao, C. Frederick, N. Traynor, J. Yang, J. Lin, M. H. Upton, D. Casa, J.-W. Kim, T. Gog, E. Karapetrova, Y. Choi, D. Haskel, P. J. Ryan, L. Horak, X. Liu, J. Liu et al., Sci. Rep. 9, 4263 (2019).

[28] D. Meyers, K. Nakatsukasa, S. Mu, L. Hao, J. Yang, Y. Cao, G. Fabbris, H. Miao, J. Pelliciari, D. McNally, M. Dantz, E. Paris, E. Karapetrova, Y. Choi, D. Haskel, P. Shafer, E. Arenholz, T. Schmitt, T. Berlijn, S. Johnston et al., Phys. Rev. Lett. 121, 236802 (2018).

[29] Z. Zhong and P. Hansmann, Phys. Rev. X 7, 011023 (2017).

[30] Y.-D. Chuang, X. Feng, A. Cruz, K. Hanzel, A. Brown, A. Spucces, A. Frano, W.-S. Lee, J. Kim, Y.-J. Chen, B. Smith, J. S. Pepper, Y.-C. Shao, S.-W. Huang, L. A. Wray, E. Gullikson, Z.-X. Shen, T. P. Devereaux, A. Tremsin, W. Yang et al., J. Electron Spectrosc. Relat. Phenom. 146897 (2019).

[31] P. E. Blöchl, Phys. Rev. B 50, 17953 (1994).

[32] J. P. Perdew, K. Burke, and M. Ernzerhof, Phys. Rev. Lett. 77, 3865 (1996).

[33] G. Kresse and J. Furthmüller, Phys. Rev. B 54, 11169 (1996).

[34] S. J. Moon, H. Jin, K. W. Kim, W. S. Choi, Y. S. Lee, J. Yu, G. Cao, A. Sumi, H. Funakubo, C. Bernhard, and T. W. Noh, Phys. Rev. Lett. 101, 226402 (2008).

[35] S. Y. Kim, C. H. Kim, L. J. Sandilands, C. H. Sohn, J. Matsuno, H. Takagi, K. W. Kim, Y. S. Lee, S. J. Moon, and T. W. Noh, Phys. Rev. B 94, 245113 (2016).

[36] W. Fan and S. Yunoki, J. Phys.: Conf. Ser. 592, 012139 (2015).

[37] S. J. Moon, M. W. Kim, K. W. Kim, Y. S. Lee, J.-Y. Kim, J.-H. Park, B. J. Kim, S.-J. Oh, S. Nakatsuji, Y. Maeno, I. Nagai, S. I. Ikeda, G. Cao, and T. W. Noh, Phys. Rev. B 74, 113104 (2006).

[38] C. Rayan Serrao, J. Liu, J. T. Heron, G. Singh-Bhalla, A. Yadav, S. J. Suresha, R. J. Paull, D. Yi, J.-H. Chu, M. Trassin, A. Vishwanath, E. Arenholz, C. Frontera, J. Železný, T. Jungwirth, X. Marti, and R. Ramesh, Phys. Rev. B 87, 085121 (2013).

[39] M. Moretti Sala, M. Rossi, S. Boseggia, J. Akimitsu, N. B. Brookes, M. Isobe, M. Minola, H. Okabe, H. M. Rønnow, L. Simonelli, D. F. McMorrow, and G. Monaco, Phys. Rev. B 89, 121101(R) (2014).

[40] A. Kotani and F. M. F. de Groot, Core Level Spectroscopy of Solids (CRC Press, Boca Raton, FL, 2008).

[41] E. Benckiser, M. W. Haverkort, S. Brück, E. Goering, S. Macke, A. Frañó, X. Yang, O. K. Andersen, G. Cristiani, H.-U. Habermeier, A. V. Boris, I. Zegkinoglou, P. Wochner, H.-J. Kim, V. Hinkov, and B. Keimer, Nat. Mater. 10, 189 (2011).

[42] J. Stohr and H. C. Siegmann, Magnetism (Springer, Berlin, 2006).

[43] D. Pesquera, G. Herranz, A. Barla, E. Pellegrin, F. Bondino, E. Magnano, F. Sanchez, and J. Fontcuberta, Nat. Commun. 3, 1189 (2012).

[44] J. M. Rondinelli, S. J. May, and J. W. Freeland, MRS Bull. 37, 261 (2012).

[45] N. A. Benedek and C. J. Fennie, Phys. Rev. Lett. 106, 107204 (2011).

[46] S. Beck and C. Ederer, Phys. Rev. Mater. 3, 095001 (2019).

[47] M. Yen, Y. Bitla, and Y.-H. Chu, Mater. Chem. Phys. 234, 185 (2019).

[48] Y. Bitla and Y.-H. Chu, FlatChem 3, 26 (2017).

[49] D. Ji, S. Cai, T. R. Paudel, H. Sun, C. Zhang, L. Han, Y. Wei, Y. Zang, M. Gu, Y. Zhang, W. Gao, H. Huyan, W. Guo, D. Wu, Z. Gu, E. Y. Tsymbal, P. Wang, Y. Nie, and X. Pan, Nature (London) 570, 87 (2019).

[50] Z. Chen, B. Y. Wang, B. H. Goodge, D. Lu, S. S. Hong, D. Li, L. F. Kourkoutis, Y. Hikita, and H. Y. Hwang, Phys. Rev. Mater. 3, 060801(R) (2019).